Chapter 11

Highlights in modern observational cosmology

Piero Rosati
European Southern Observatory, Garching b. München,
Germany

11.1   Synopsis

In this chapter, we focus on the fundamental methods of observational cosmology and summarize some of the recent observational results which have deepened our understanding of the structure and evolution of the universe. The chapter is divided into three parts. In the first section, we briefly describe the Friedmann world models, which constitute the theoretical framework, we define the main observables and we illustrate some common applications. In the second section, we describe how galaxy surveys (primarily in the optical band) are utilized to map the structure and evolution of the universe over a large fraction of its age, focusing on observational methodologies and some recent results. In the third section, we describe how surveys of galaxy clusters can be used to constrain cosmological models, and measure the fundamental cosmological parameters. Throughout the chapter, we touch *only* on a few recent highlights in observational cosmology. We refer the reader to fundamental textbooks, such as Longair (1998), Peebles (1993) and Peacock (1999), for a complete overview of the theoretical and observational framework.

11.2   The cosmological framework

This section gives a very brief summary of the basics of Friedmann–Robertson–Walker (FRW) models; only the essentials formulae which are used throughout the chapter and the definition of observable quantities which are often used in cosmology are included.

11.2.1   Friedmann cosmological background

What is generally referred to as the *standard cosmological framework* is the result of the solution of the Einstein equations in the hypothesis that the universe is, *on very large scales*, *homogeneous* and *isotropic*. There are several pieces of observational evidence which support this *cosmological principle*, such as the distribution of galaxies and clusters of galaxies on large scales and the remarkable isotropy of the cosmic microwave background (CMB).

The FRW models provide the *background* on which the formation and evolution of the large-scale structure in the universe can be studied as the evolution of small perturbations to an otherwise uniform FRW model. The application of the cosmological principle leads to the following FRW spacetime line element (see Landau and Lifshitz (1971) for an elegant and simple derivation):

$$ds^2 = c^2\,dt^2 - R^2(t)\left[\frac{dr_1^2}{1 - kr_1^2} + r_1^2(d\theta^2 + \sin^2\theta\,d\phi^2)\right] \quad (11.1)$$

$$= c^2\,dt^2 - R^2(t)[dr^2 + S_k^2(r)(d\theta^2 + \sin^2\theta\,d\phi^2)] \quad (11.2)$$

where two possible definitions of the *comoving coordinate, r,* have been used. This is the coordinate measured by observers at rest with respect to the local matter distribution. The first expression is commoonly used in the literature. In the second form, following the notation by Peacock (1999), we have defined:

$$S_k(r) = \begin{cases} \sin(r) & k = 1 \text{ (close)} \\ r & k = 0 \text{ (flat)} \\ \sinh(r) & k = -1 \text{ (open)}. \end{cases} \quad (11.3)$$

The cases $k = -1, 0, 1$ represent, respectively, an *open universe* (infinite, hyperbolic space), a *flat universe* (infinite, flat space) and a *closed universe* (finite, spherical space).

The solution of the Einstein field equations (with cosmological constant Λ) leads to the following equation for the evolution of the scale factor, $R(t)$:

$$\left(\frac{\dot{R}}{R}\right)^2 = \frac{8\pi G}{3}\rho_M + \frac{1}{3}\Lambda c^2 - \frac{kc^2}{R^2}. \quad (11.4)$$

This shows three competing terms driving the universal expansion: a matter term, a cosmological constant term and a curvature term. We are neglecting here a radiation term, as appropriate when the universe is dominated by non-relativistic matter ('dust') with density ρ_M, i.e. the directly observable universe. The respective fractional contributions to the energy density in the universe at the present epoch are commonly defined as

$$\Omega_m \equiv \frac{8\pi G}{3H_0^2}\rho_{M_0}, \qquad \Omega_\Lambda \equiv \frac{\Lambda c^2}{3H_0^2}, \qquad \Omega_k \equiv -\frac{kc^2}{H_0^2 R_0^2} \quad (11.5)$$

with

$$\Omega_m + \Omega_\Lambda + \Omega_k = 1, \qquad \Omega_{tot} = \Omega_m + \Omega_\Lambda = 1 - \Omega_k \qquad (11.6)$$

where $H_0 \equiv (\dot{R}/R)_{t=0} = 100 \text{ km s}^{-1} \text{ Mpc}^{-1} h = h(9.78 \times 10^9)^{-1}$ years, is the present value of the *Hubble constant*. The matter density parameter, Ω_m (sometimes denoted as Ω_0), can also be written as $\Omega_m = \rho_0/\rho_{cr}$, where $\rho_{cr} = 3H_0^2/(8\pi G) = 1.9 \times 10^{-29}h^2 \text{ g cm}^{-2}$ is the critical density, which splits open and close models in a matter-dominated universe.

The *deceleration parameter* is also often used:

$$q \equiv -\ddot{R}R/\dot{R}^2 = \Omega_m/2 - \Omega_\Lambda. \qquad (11.7)$$

With these definitions, the equation (11.4) can be written:

$$H^2 = H_0^2 \left[\Omega_m \left(\frac{R_0}{R} \right)^3 + \Omega_k \left(\frac{R_0}{R} \right)^2 + \Omega_\Lambda \right]. \qquad (11.8)$$

11.2.2 Observables in cosmology

Suppose we are at $r = 0$ and observe an object at radial coordinate r_1, when the expansion factor was $R_1 = R(t_1) < R_0$, at some lookback time $t_1 < t_0$. Quantities like r_1, t_1, R_1 are not accessible to measurement. However, there are directly measurable quantities which can be used to test the validity of the FRW metric and to derive its parameters.

First of all, the *redshift*. From the spectrum of a distant source we can easily recognize, say, an emission line whose rest-frame (emitted) wavelength is λ_e. In general, we will measure a redshifted emission line at wavelength λ_0, so that the *redshift z* is defined as

$$1 + z = \frac{\lambda_0}{\lambda_e}. \qquad (11.9)$$

If the expansion factor of the universe was R at redshift z, the following simple relation holds:

$$1 + z = \frac{R_0}{R}. \qquad (11.10)$$

Using this relation, we can now immediately write the *lookback time*, $\tau(z)$, by integrating equation (11.8) after a change of variable, from R to z:

$$\tau(z) = H_0^{-1} \int_0^z (1 + z')^{-1} [\Omega_k(1 + z')^2 + \Omega_m(1 + z')^3 + \Omega_\Lambda]^{-1/2} \, dz'. \quad (11.11)$$

$\tau(z)$ is plotted in figure 11.1 for three different values of $(\Omega_m, \Omega_\Lambda)$. The age of the universe is obtained for $z \to \infty$.

We now examine the other measurable quantities.

11.2.2.1 Angular diameters

Photons from our distant object at radial distance r follow radial, null geodesics ($ds^2 = 0$). Using the FRW metric (11.2), we can then link the angular size ($\Delta\theta$) of an object to its proper length d, perpendicular to the radial coordinate at redshift z:

$$d = R S_k(r)\Delta\theta = R_0 S_k(r)\Delta\theta/(1+z)$$
$$\Delta\theta = \frac{d(1+z)}{d_M} = \frac{d}{D_A} \tag{11.12}$$

where we have defined the *distance measure*, $d_M \equiv R_0 S_k(r)$, and the *angular diameter distance* $D_A = d_M/(1+z)$.

The distance measure out to redshift z, $d_M(z)$, can be derived integrating the equation of motion for a photon, $R\,dr = c\,dt = c\,dR/(RH)$, and using the equations (11.8) and (11.10):

$$
\begin{aligned}
d_M(z) &= \frac{cH_0^{-1}}{|\Omega_k|^{1/2}} S\left\{ |\Omega_k|^{1/2} \int_0^z [\Omega_k(1+z')^2 + \Omega_m(1+z')^3 + \Omega_\Lambda]^{-1/2}\,dz' \right\} \\
&= \frac{cH_0^{-1}}{|\Omega_k|^{1/2}} S\left\{ |\Omega_k|^{1/2} \int_0^z [(1+z')^2(1+\Omega_m z') - z'(2+z')\Omega_\Lambda]^{-1/2}\,dz' \right\}
\end{aligned}
\tag{11.13}
$$

where the multiple function S is defined in (11.3); in the flat case of $\Omega_k = 0$ only the integral remains. Such an integral can easily be evaluated numerically.

For $\Omega_\Lambda = 0$, an analytical solution exists (Mattig 1957):

$$d_M = \frac{2cH_0^{-1}}{\Omega_0^2(1+z)}\{\Omega_0 z + (\Omega_0 - 2)[(\Omega_0 z + 1)^{1/2} - 1]\}. \tag{11.14}$$

Equation (11.12) shows that if a 'standard rod' existed, e.g. a class of objects associated with a fixed physical size with negligible evolutionary effects, then it would be possible to infer cosmological parameters (particularly q_0) by plotting the angular size as a function of redshift (e.g. Kellerman 1993).

11.2.2.2 Apparent intensities

If L is the *rest-frame luminosity* of an object at redshift z (in a given band), then its flux (measured in erg cm^{-2} s^{-1} in cgs units) is

$$S = \frac{L}{4\pi d_M^2(1+z)^2} = \frac{L}{4\pi D_L^2} \tag{11.15}$$

where $D_L = d_M(z)(1+z)$ is the so called *luminosity distance* of the source, which is defined so that the flux assumes the familiar expression in Euclidean

geometry (inverse square law). Observations (i.e. fluxes, luminosities) in a given band $[\nu_1, \nu_2]$ can be related to the rest-frame band through the computation of the *K-correction*, K_z, which is essentially the ratio of fluxes in the rest-frame to the observed (redshifted) band $[(1 + z)\nu_1, \nu_2(1 + z)]$. In optical astronomy the magnitude system is used ($m \sim -2.5 \log(S)$) so that (11.15) can be written as a relation between the apparent (m) and absolute magnitude (M) of the object:

$$m = M + 5 \log \left(\frac{D_L}{10 \text{ pc}} \right) + K_z. \tag{11.16}$$

If the flux spectra density is a power law, i.e. $f_\nu \sim \nu^{-\alpha}$ (like most of the galaxies), then one easily obtains $K_z = 2.5(\alpha - 1) \log(1 + z)$. Such a term can add up to several magnitudes for early type (i.e. red) galaxies at $z \sim 1$.

A low redshift expansion of (11.16) leads to the simple formula (e.g. Sandage 1995):

$$m = 5 \log z + 1.086(1 - q_0)z + 5 \log c H_0^{-1} + M + 25. \tag{11.17}$$

This shows that if we can recognize a class of astrophysical sources as 'standard candles', by measuring the dimming of these sources over a wide range of redshifts we can measure the deceleration parameter, q_0, and eventually separate Ω_m and Ω_Λ. The application of this fundamental test to high redshifts Type Ia supernovae has lead to spectacular results in recent years (e.g. Perlmutter *et al* 1999, Schmidt *et al* 1998).

11.2.2.3 Number densities

One of the main goal of redshift surveys is to quantify the comoving volume density of objects as a function of redshift. A frequently used quantity is therefore the *comoving volume element* in the redshift interval, z to $z+dz$, in the solid angle $d\Omega$, which follows directly from the FRW metric (11.1), (11.2):

$$dV = \frac{d_M^2}{(1 + \Omega_k c^{-2} H_0^2 d_M^2)^{1/2}} d(d_M) \, d\Omega. \tag{11.18}$$

Using equation (11.13), and defining the functions $E(z)$ and $A(z)$ as

$$E(z) = \int_0^z [\Omega_k(1 + y)^2 + \Omega_m(1 + y)^3 + \Omega_\Lambda]^{-1/2} \, dy \equiv \int_0^z A(y) \, dy,$$

we have:

$$\frac{dV}{d\Omega \, dz} = (c H_0^{-1})^3 A(z) |\Omega_k|^{-1} S^2 \{ |\Omega_k|^{1/2} E(z) \} \tag{11.19}$$

$$= c H_0^{-1} A(z) d_M^2 \equiv Q(z, \Omega_m, \Omega_\Lambda),$$

where, as usual, we defined S^2 as $\sinh^2$ if $\Omega_k > 0$ (open universe) and $\sin^2$ if $\Omega_k < 0$ (close universe). In the flat case, $S^2 \to E^2(z)$. Remember that Ω_k is not an independent parameter but rather given by $1 - \Omega_m - \Omega_\Lambda$.

For $\Omega_\Lambda = 0$, one finds:

$$\frac{dV}{d\Omega \, dz} = \frac{(cH_0^{-1})^3}{(1+z)^3} \frac{\{q_0 z + (q_0 - 1)[(2q_0 z + 1)^{1/2} - 1]\}^2}{q_0^4 (1 + 2q_0 z)^{1/2}} \tag{11.20}$$

$cH_0^{-1} \simeq 3000h^{-1}$ Mpc is the Hubble length.

The volume element (11.19) is plotted in figure 11.1 for three reference models. We will see later that the flat case $(\Omega_m, \Omega_\Lambda) = (0.3, 0.7)$ is currently favoured by measurements. This plot shows that if we peer into a patch of the sky with deep observations, at $z = 2$–3 we have a good chance to explore a large comoving volume (which is ultimately determined by the observational technique).

11.2.2.4   Surface brightnesses

The observed surface brightness Σ_{obs} of an extended object is defined as the flux per unit emitting area. This is the observable that ultimately drives the detection of faint galaxies (rather than its flux), and has the remarkable property of being independent on cosmological parameters. For a FRW model, using equations (11.15), (11.12), it is:

$$\Sigma_{obs} = \frac{S_{obs}(\nu_1, \nu_2)}{\pi \Theta^2} = \frac{L_{obs}(\nu_1, \nu_2) K_z}{4\pi d_M^2} \frac{d_M^2}{\pi d^2 (1+z)^4} = \frac{1}{\pi} \left(\frac{L_{obs}}{4\pi d^2} \right) \frac{K_z}{(1+z)^4}.$$

This is also known as the Tolman law, and can be used as a direct test of the expansion of the universe (e.g. Sandage 1995). $L_{obs}/4\pi d^2$ is the intrinsic surface brightness of the source with physical size d (in units of, e.g., erg s^{-1} kpc^{-2}). Besides the K-correction, this relation shows that the surface brightness of extended objects drops very rapidly with redshifts, making the detection of high-z extended objects difficult.

11.2.3   Applications

One of the most common application of the expressions derived in the previous section is the computation of observed distributions, such as source number counts, or the redshift-dependent volume density of a class of objects, based on known local ($z \simeq 0$) distributions. By comparing these observed distributions, at different redshifts, with those predicted on the basis of observations in the local universe or models of structure formation, one can set constraints on the evolutionary history of a given class of objects, and, *in principle*, on the cosmological model itself (i.e. on Ω_m, Ω_Λ).
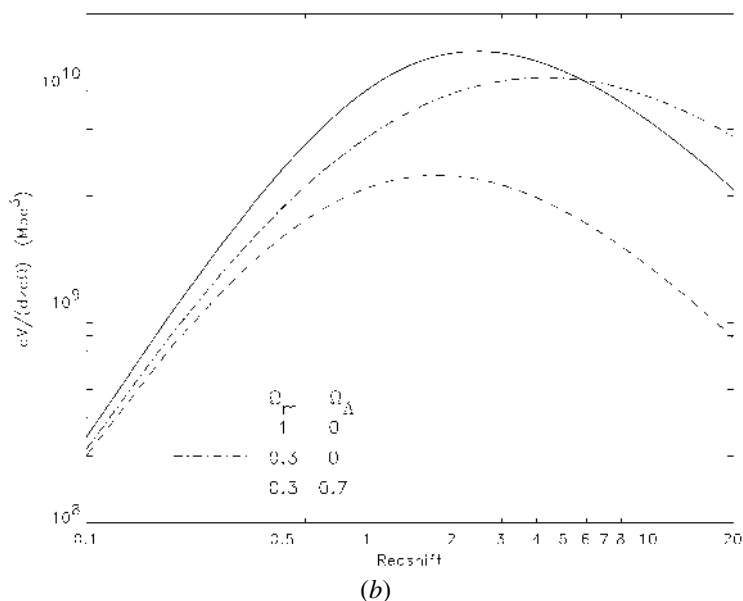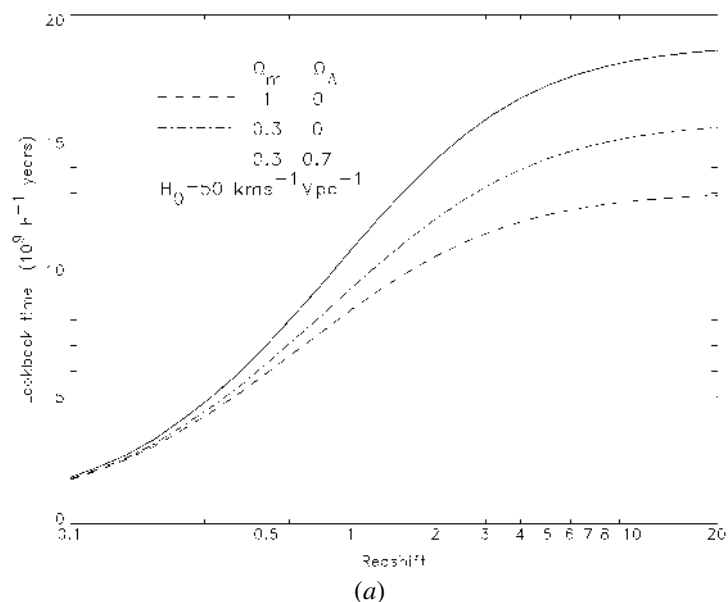
Figure 11.1. (*a*) Lookback time as a function of the redshift for three reference FRW models (Einstein–de Sitter, open, flat). At $z = 20$ the lookback time is approximately 99% of the age of the universe in all models. (*b*) Derivative of the comoving volume element, per unit solid angle, as a function of redshift for the same models.

11.2.3.1   Number counts

By number counts we mean the surface density on the sky of a given class of sources as a function of the limiting flux of the observations (e.g. magnitude, radio flux). This is the simplest observational tool which can be used to study the evolution of a sample of objects, and, to some extent, to test cosmological models. It does not require redshift measurements but only a knowledge of the selection function (indeed, a major challenge in any survey in comology!).

The space density of sources of different intrinsic luminosities, L, is described by the *luminosity function* (LF), $\phi(L)$, so that $dN = \phi(L) dL$ is the number of sources per unit volume with luminosity in the range L to $L + dL$. The most common functional form to describe observational data is the one proposed by Schechter (1976):

$$\phi(L) = \frac{\phi_*}{L_*} \left(\frac{L}{L_*} \right)^{-\alpha} e^{-L/L_*}. \tag{11.21}$$

L_* is the *characteristic luminosity* of the population, the normalization ϕ_* determines the volume density of sources, as $n_0 = \int_0^\infty \phi(L) dL = \phi_* \Gamma(1 - \alpha)$, where Γ is the gamma-function. The product $\phi_* L_*$ is an estimate of the integrated luminosity of all sources in a given volume, since the *the luminosity density* is defined as $\epsilon_L = \int_0^\infty L\phi(L) dL = \phi_* L_* \Gamma(2 - \alpha)$.

The determination of the local LF of galaxies is not completely straighforward since one has to take into account the morphological mix of galaxies (i.e. the existence of a variety of morphological types, from ellipticals to spirals and irregulars) and clustering effects which bias the measurement of the space density. Most of the observations in the nearby universe (e.g. Loveday *et al* 1992) find best-fit parameters:

$$L_* \simeq 10^{10} h^{-2} L_\odot$$

(corresponding to a B band absolute magnitude $M_B \simeq 20 + 5 \log h$);

$$\phi_* \simeq (1.2\text{--}1.5) \times 10^{-2} h^3 \text{ Mpc}^{-3}, \qquad \alpha \simeq 1.$$

Let us consider, for simplicity, the local or nearby Euclidean universe uniformly filled with sources with LF $\phi(L)$. If S is the limiting flux, sources with luminosity L can be observed out to $r = (L/4\pi S)^{1/2}$. The number of sources over the solid angle Ω, observable down to the flux S are:

$$N(> S) = \int \frac{\Omega}{3} r^3 \phi(L) dL = \frac{\Omega}{3(4\pi)^{3/2}} S^{-3/2} \int L^{3/2} \phi(L) dL.$$

Once the integral over all luminosities is evaluated, the surface density of sources down to the flux S is always $N(> S) \propto S^{-3/2}$. If we use magnitude instead of luminosities, then $\log N(> m) \propto 0.6 \, m$. Therefore, number counts in

the nearby universe, where curvature terms can be neglected, are characterized by a *Euclidean slope* of -1.5 (or 0.6 mag). In general, at large distances, curvature effects (cf equations (11.13) and (11.18)) cause number counts to have slopes always shallower than the Euclidean one. However, as we will see in section 11.3.3, evolutionary effects ($\phi = \phi(L, z)$) can counteract such a natural behaviour and produce counts steeper than 1.5.

11.2.3.2 Redshift distribution and number counts (general case)

We now have all the ingredients to compute the expected redshift distribution, $n(z)$, and number counts, $n(> S)$, for an evolving population of sources with LF $\phi(L, z)$. Typically, on the basis of the known local LF, $\phi(L, 0)$, one wants to compare the *observed* redshift distribution of sources with the one expected on an empirical evolutionary scenario, or the one predicted by some theory of structure formation. In general, there will be some degree of degeneracy between evolutionary parameters and cosmological paramaters (Ω_m, Ω_Λ) when matching theoretical models with observational data.

With $Q(z, \Omega_m, \Omega_\Lambda)$ given by equation (11.19) (or (11.20)), the number of sources per unit solid angle and redshift, in the luminosity range L to $L + dL$, is:

$$\frac{d^2 N}{d\Omega dz} \phi(L) \, dL = Q(z, \Omega_m, \Omega_\Lambda) \frac{\phi_*}{L_*} \left(\frac{L}{L_*}\right)^{-\alpha} e^{-L/L_*} \, dL. \tag{11.22}$$

We now change variable, $y = L/L_*$, and call L_1 and L_2 the minimum and maximum luminosity of the source population (for example, a magnitude range within which we want to compute the redshift distribution). Thus, the surface density of sources, per unit redshift, observed down to the flux S can be written as:

$$\frac{dN(> S, z)}{d\Omega \, dz} = \phi_* Q(z, \Omega_m, \Omega_\Lambda) \int_{y_1(z)}^{y_2} y^{-\alpha} e^{-y} \, dy \tag{11.23}$$
$$= \phi_* \Gamma(1 - \alpha) Q(z, \Omega_m, \Omega_\Lambda)[P(1 - \alpha, y_2) - P(1 - \alpha, y_1)],$$

where P is the generalized Γ-function, $y_2 = L_2/L_*$, and

$$y_1(z) = \max\left(\frac{L_1}{L_*}, \frac{L_{min}(S, z)}{L_*}\right), \qquad L_{min}(S, z) = S 4\pi D_L^2(z) K_z. \tag{11.24}$$

L_{min} is the rest-frame miminum luminosity detectable at redshift z, at the limiting flux S (equation (11.15)).

The numerical integration of equations (11.23) and (11.24) can also include an evolving LF, e.g. $\phi_* = \phi_*(z)$, $L_* = L_*(z)$. The result can be directly compared with the observed redshift distribution of sources, i.e. the number of sources per deg^2, in each redshift bin. The number counts $n(> S)$ are obtained by integrating (11.23) over all redshifts.

11.3   Galaxy surveys

11.3.1   Overview

Over the last ten years, significant progress has been made in both observational and theoretical studies aimed at understanding the evolutionary history of galaxies, the physical processes driving their evolution and leading to the Hubble sequence of types (ellipticals, spirals, irregulars) that we observe today.

Deep galaxy surveys have had a central role in cosmology back to the pioneering work of Hubble. In the 1960s (see Sandage 1995) several studies used galaxy counts as a tool to test cosmological models; however, it was soon realized that it was difficult to disentangle the effects of *evolution* from those due to the *universal geometry*, as well as the effects of *object selection*, which, if not properly understood, can easily alter the slope of the number counts (see later).

The modern era of observational cosmology began with the advent of CCD detectors in the 1980s and soon after with multi-object spectrographs. Scientific progress has obviously been driven by a series of technological breakthroughs with telescopes and instrumentation, that we can summarize as follows:

- *Mid 1980s*: First deep CCD surveys (Tyson 1988) revealed a large number of faint, blue galaxies in nearly confusion limited images.
- *Early 1990s*: (a) the development of multi-object spectrographs allows the first spectroscopic surveys of distant galaxies (e.g. Ellis *et al* 1996, Lilly *et al* 1995); and (b) central role of Hubble Space Telescope (HST) (resolved images of distant galaxies, morphological information).
- *Mid 1990s*: (a) spectroscopy with the Keck telescope (10 m collecting area) pushed the limit to two magnitudes fainter; (b) significant improvement in near-IR imaging (sensitivity and detector area); and (c) deep imaging in the millimetre wavelength with the SCUBA instrument.
- *Late-1990s*: wide-field optical imaging; (b) high-multiplexing spectroscopy (several hundreds of spectra at once); and (c) 8 m class telescopes with active optics (VLT) (delivering angular resolution of $0.5''$ or better).
- *On-going/upcoming*: (a) next generation of spectrographs + near-IR spectroscopy on 8–10 m class telescopes; (b) Integral-field spectrographs (x, y, λ information); (c) adaptive optics delivering diffraction-limited images ($\sim 0.05''$ resolution); and (d) Advance Camera for Survey on HST (2001).

This rapid technological development has allowed a number of major surveys to be carried out. We can classify those which have had a major impact on the way we understand the structure and evolution of the universe today as follows:

Large area surveys

- APM (Automatic Plate-measuring Machine, e.g. Maddox *et al* 1990)—imaging photographic plates;
- CfA survey (Center for Astrophysics, e.g. Huchra *et al* 1990);
  LCRS (Las Campanas Redshift Survey, e.g. Shectman *et al* 1996)—$\sim 10^4$ galaxy redshifts, over 700 deg^2 out to $z \simeq 0.2$;
- 2dF survey (2 degree field, e.g. Colless 1999)—$\sim 10^5$ redshifts covering 1700 deg^2; and
- SDSS survey (Sloan Digital Sky Survey: http://www.sdss.org)—$\sim 10^6$ redshifts + multicolour imaging (10^4 deg^2, $m_{\lim} \simeq 22$).

The first three surveys have provided the power spectrum of the large-scale structure, by measuring the correlation function over a wide range of scales (see L Guzzo, this volume), and the luminosity functions of different galaxy types in the local universe. The on-going 2dF and SDSS surveys will soon bring these measurements to an unprecedented level of precision.

Deep, small area surveys

- The LDSS autofib survey (Ellis *et al* 1996)—B-band selected redshift survey down to $B \simeq 24$ ($z \lesssim 0.7$).
- The CFRS survey (Lilly *et al* 1995)—I-band selected redshift survey down to $I \simeq 22$ (~ 600 galaxies at $z \lesssim 1$).
- The Keck Survey (Cowie *et al* 1996)—150 galaxy redshifts out to $z \simeq 1.5$ ($22.5 < B < 24$).
- The CNOC2 surveys (Yee *et al* 2000)—6000 galaxy redshifts over 1.5 deg^2 area ($z \lesssim 0.6$).

These surveys have established a clear evolutionary pattern for different galaxy types out to $z \sim 1$ (see section 11.3.3).

Ultra-deep, tiny area surveys

- Hubble Deep Field North and South (e.g. Williams *et al* 1996, Ferguson *et al* 2000)—5 arcmin^2, $m_{\lim} \simeq 29$ (see later).

11.3.2 Survey strategies and selection methods

When planning an imaging survey (not necessarily in optical or near-IR wavelengths which are the primary subject here), the balance between the *depth* and the *solid angle*, as well as the selection of the *observed band* play a central role. These decisions are driven by the nature of the sources under study, as well as their typical volume density and luminosity, i.e. ϕ_* and L_* (see (11.21)). Rare objects, such as quasars or galaxy clusters, require large-area surveys to be found in sizeable numbers. Large surveys also probe the bright end of the LF
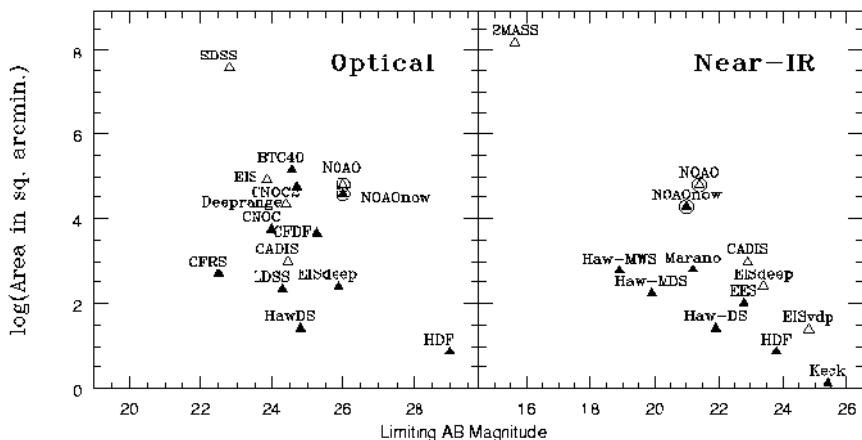
Figure 11.2. Several optical and near-IR surveys (carried out over the last ten years) in the depth–solid angle plane. The AB magnitude system is defined as $m(\text{AB}) = -2.5 \log f_\nu(\text{nJy}) + 31.4$.

of any source population, as opposed to small-area surveys which mostly probe the faint end of the LF ($L \lesssim L_*$). In general, the deeper the survey is the more distant are the L_* objects which can be detected. The combination depth–solid angle will determine the sampled volume at different redshifts, for a given object selection method. Obviously, the product (limiting flux × survey area) is kept approximately constant by observational time constraints. In figure 11.2, we plot several cosmological surveys which have been carried out over the last ten years with the aim of mapping the structure in the universe and understanding its evolution. The Sloan Digital Sky Survey (SDSS) and the Hubble Deep Field (HDF) represent the two complementary extremes, i.e., a shallow survey covering a significant fraction of the sky and a very deep pencil beam survey.

For a given depth and survey area, the probed volume is ultimately determined by the *selection function*, i.e. the set of criteria which lead to the object detection. There are basically three different selection methods:

(1) *Flux-limited selection.* All the sources with a flux greater than a given threshold, S_{lim}, are included in the sample. The simplicity of this method leads to a straightfoward computation of the probed volume (however, see caveats later). If A_S is the survey area, the maximum redshift, z_{max}, at which a source of rest frame luminosity L can be detected, is given implicitily by $L = S_{\text{lim}} 4\pi D_L^2(z_{\text{max}})$ (11.15). Thus, using (11.19), the *survey volume* is:

$$V_{\text{max}}(z, L) = A_S \int_0^{z_{\text{max}}} Q(z, \Omega_{\text{m}}, \Omega_\Lambda) \, \text{d}z. \qquad (11.25)$$

Note that the K-correction is also involved in this calculation when

converting from observed to rest-frame luminosities. By counting sources in different luminosity–redshift bins one can thus estimate the LF $\phi(z, L)$.

(2) *Colour selection*. Sources are selected on the basis of their flux *and* colour. A relevant case is described in section 11.3.4. The advantage of this method is that it is extremely efficient at isolating objects in a given redshift range, for example a distant volume in the universe. However, the selection function (i.e. the survey volume) critically depends on the knowledge of the spectral energy distribution (SED) of the sources under study.

(3) *Narrow-band filter selection*: This technique consists of selecting sources which have a flux excess when observed through a narrow-band filter, as compared to their broad-band flux. Emission line objects (e.g. starbursts, AGN) are the targets of these surveys. Sources are detected at redshift $1 + z = \lambda_{\text{filter}}/\lambda_{\text{em.line}}$, within a Δz given by the width of the filter, which needs to be narrow enough ($\lesssim 100$ Å) to boost the contrast of the emitting line object against the background sky. The equivalent width of the emission line ultimately determines the selection function. Several searches for very high redshifts objects have been conducted using the Lyα (1216 Å) as a tracer. Such surveys have had some success (Hu *et al* 1999), but have also underscored the difficulties of this method. First, a very narrow redshift slice is probed, and therefore samples are small and prone to cosmic variance and large-scale structure effects. Second, only a limited portion of the galaxy population (e.g., galaxies with large equivalent width) is selected. These limitations make it difficult to draw statistical conclusions on the volume density, or luminosity density of distant galaxies.

11.3.2.1 Caveats

There are several caveats inherent in the aforementioned selection methods, which if not properly addressed, can lead to a biased view of the evolution of the structure in the universe and underlying cosmological models.

First of all, the flux-limit approach is an idealization of our detection process. Sources are never detected on the basis of their flux, but rather on the basis of their surface brightness (a detection consists of an excess of flux within a given aperture, above a given threshold, which is usually a few times the rms value of the surrounding background). A major concern of any survey is to establish whether the sample is, to a good approximation, *flux-limited* rather than *surface-brightness-limited*. As a result, the flux limit (S_{lim}) should be chosen high enough so to cover the whole range of surface brightness of our sources. Low surface brightness sources will be the first to drop out of the sample if this process is ill defined.

Second, the computation of the *K-correction* requires a knowledge or assumptions on the SED of sources at different redshifts.

Third, the effect of *reddening* especially due to dust enshrouding distant objects (and, to a lesser extent, to intervening neutral hydrogen) can have a
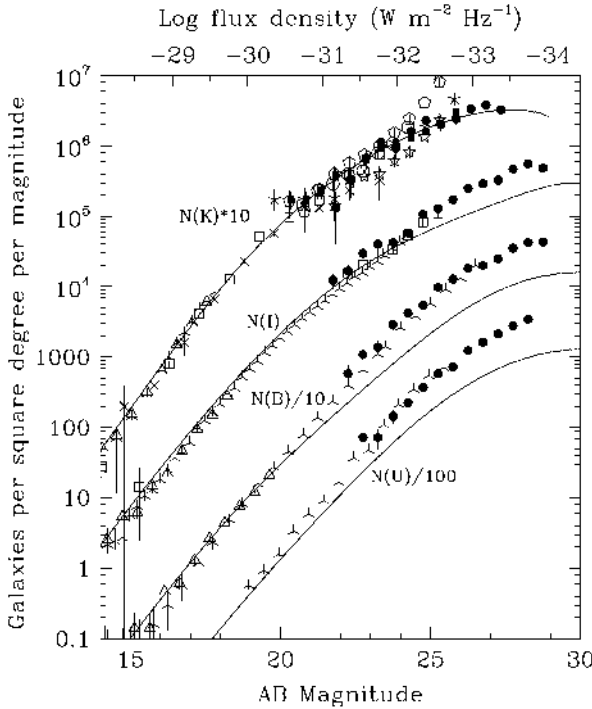
Figure 11.3. A compilation of number counts in the U, B, I, K bands from different surveys (Ferguson *et al* 2000 and references therein). Full symbols are from the HDF North and South, open symbols from several ground-based surveys. Full lines are no-evolution models obtained integrating the observed local luminosity function for $(\Omega_{\mathrm{m}}, \Omega_{\Lambda}) = (0.3, 0.7)$.

significant impact on the selection function and completeness of the sample by absorbing the UV part of the continuum and selectively suppressing different emission lines.

11.3.3 Galaxy counts and evolution

We show in figure 11.3 a compilation of number counts from ground-based and HST surveys over a 13 magnitude range, as observed in the U, B, I and K passbands (see Ferguson *et al* 2000). Each set is displaced by a factor of 10 for clarity. Full curves represent the theoretical expectations obtained by integrating the local luminosity function assuming *no evolution* and $(\Omega_{\mathrm{m}}, \Omega_{\Lambda}) = (0.3, 0.7)$, as described in section 11.3.3. These no-evolution (NE) models make reasonable assumptions on the morphological mix of the local galaxy population (relative fraction of irregulars, spirals, ellipticals), their LFs and their SEDs (required to

compute the K-corrections). Such assumptions reflect observations of the nearby universe but are still affected by some uncertainty, therefore it is not uncommon to find in the literature NE models which differ by $\sim$50%. This uncertainty will be drastically reduced when the 2dF and SDSS surveys are completed.

A clear trend is apparent in figure 11.3. At blue wavelengths the observed counts exceeds the NE predictions by as much as a factor three, a problem which was recognized in the first deep surveys and which has become known as the *faint blue galaxy excess*. Such an excess progressively disappear at longer wavelengths. Observations in blue filters are sensitive to late type, star-forming galaxies with young stellar populations. Therefore, it had already become evident in the early 1990s (e.g. Ellis *et al* 1996) that this is the galaxy population which has undergone most of the evolution (in luminosity and/or number density) out to $z \sim 1$, i.e. the last 50% of the life of the universe. The first deep redshift surveys (Lilly *et al* 1995) confirmed this scenario directly measuring a significant evolution of the LF for the 'blue population' out to $z \simeq 0.7$, while revealing no significnt evolution for the 'red population' consisting of galaxy types earlier than an Sbc (see figure 11.4). Red wavelength observations, particularly in the K-band ($\lambda_0 = 2 \ \mu$m), collect rest-frame optical light out to $z \sim 3$, thus probing old, long-lasting stellar populations in distant galaxies (i.e. earlier types). All these observations (see also Cowie *et al* 1996) have shown a remarkable increase in the space and/or luminosty density of star-forming galaxies with redshift. However, interpreting these results, and understanding the physical processes responsible for this evolutionary pattern, has remained a difficult task.

In this respect, HST observations have driven us a big step forward by allowing *intrinsic sizes* and *morphologies* of distant galaxies to be measured. The combination of angular resolution (0.05$''$) and depth has also pushed these studies well beyond $z = 1$. As an example, in figure 11.5 we show number counts for different morphological types as directly determined by the HDF-N images (Driver *et al* 1998). Along with NE model predictions (full lines), *passive evolution models* are also shown. The latter are constructed using spectral synthesis models (e.g. Bruzual and Charlot 1993), assuming a formation redshift (generally varying by type), and a star formation history (with a given initial mass function, IMF). As an example, in figure 11.6 we show the evolution of the SED of a 3 Gyr burst stellar population over approximately a Hubble time. This model well reproduces the evolution of an early type galaxy. The UV luminosity declines rapidly after the end of the burst of star formation, as hot O and B stars burn off the main sequence and the population is more and more dominated by red giants.

In general, passive evolution models are characterized by *luminosity evolution*, which is the result of letting the stellar populations evolve with a pre-defined star formation history, without including any merging. Figure 11.5 confirms that morphologically selected early types show little (simple passive) evolution to faint magnitudes, and hence to relatively high redshifts. Counts of intermediate types (i.e. spiral-like galaxies) are broadly consistent with passive, luminosity evolution models, whereas later types and irregulars are not fitted by
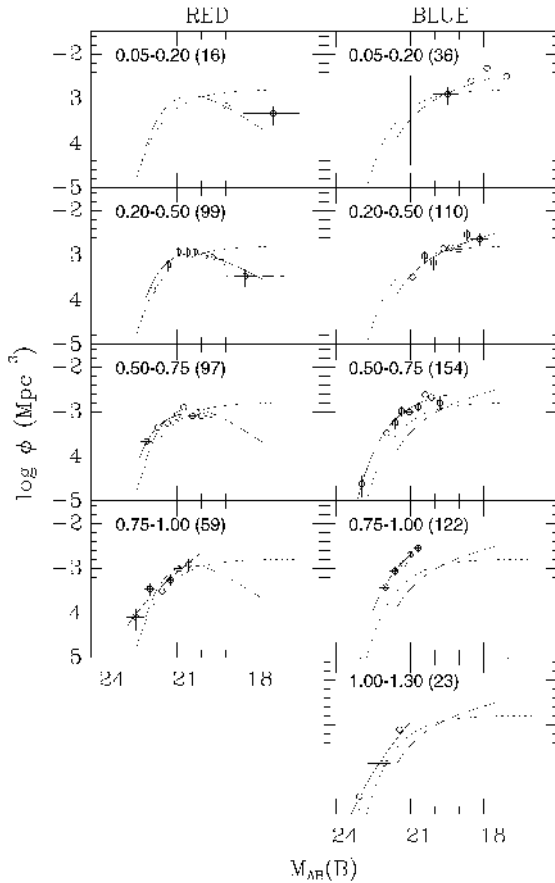
Figure 11.4. Measurement of the LF at different redshifts from the CFRS survey (Lilly *et al* 1995). The redshift bin and number of objects for each LF are given in the label in each panel. The dividing line between 'red' and 'blue' samples corresponds to the rest-frame colour of an Sbc galaxy. A clear evolution is visible in the blue sample, whereas no significant evolution is observed in the red sample out to $z \simeq 0.7$.

any of these models. It is believed that most of the morphological evolution of these irregular and peculiar galaxies occurs at $1 \lesssim z \lesssim 2$, as a result of interactions or merging, to lead to the assembling of the familiar Hubble sequence. In general, fairly complex luminosity evolution models, which also include a prescription for dust obscuration, fail to predict number counts at the faintest magnitudes or the number density of galaxies at $z \gtrsim 2$. This is a clear indication that a much deeper physical understanding of the galaxy formation processes is needed ('active' versus simple passive evolution). Central, unsolved key questions are how the star formation activity is modulated by merging and
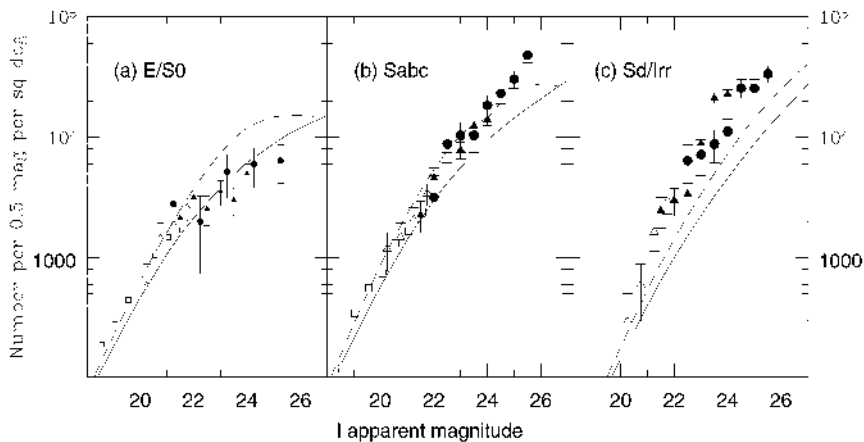
Figure 11.5. Number counts for different morphological types as derived from the HDF-N survey (Driver *et al* 1998). The full and broken curves are predictions from no-evolution and passive evolution models respectively (for $\Omega_m = 1$, $\Omega_\Lambda = 0$).

how the stellar mass is assembled over time in a hierarchical structure formation scenario.

11.3.4 Colour selection techniques

The measurement of the redshift of distant (say $z > 1$), faint galaxies is a time-consuming task and becomes impossible at magnitudes fainter than ~ 25, even with 8–10 m class telescopes equipped with modern spectrographs. As outlined in section 11.3.3, statistical studies of the nature and evolution of galaxies require an estimate of their SED and their redshift at magnitude selections well beyond the spectroscopic limit. This has stimulated intensive activity over the last few years, aimed at exploiting *colour selection techniques* to *isolate and study* galaxy populations at different redshifts. The basic idea has been to use multi-colour imaging, in as many passbands as possible, to constrain the SED of galaxies by detecting spectral features and measuring the continuum slope, thus estimating the redshift.

The most successful colour selection method in recent years, which has become known as *Lyman break technique*, was devised to detect the ubiquitous Lyman limit discontinuity at 912 Å, which is redshifted into the HST bandpasses at $z \gtrsim 2$ (or at $z \gtrsim 2.5$ for redder ground-based filters) (e.g. Steidel *et al* 1996). This technique is illustrated in figure 11.7 (see the review by Dickinson 1998). A galaxy with an unreddened UV continuum (i.e. a star-forming galaxy or an AGN) has a nearly flat spectrum in f_ν, and a sharp break due to photolectric absorption of intervening neutral hygrogen (in the galaxy itself and in the intergalctic space along the line of sight) shortward of 912 Å (lyman limit). The integrated effect
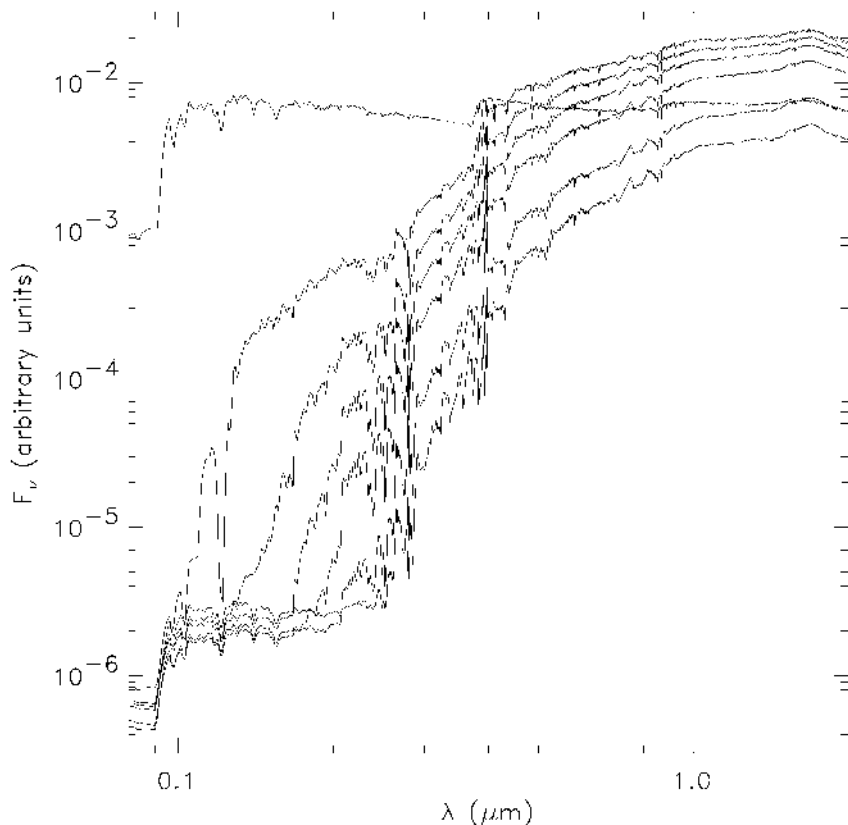
Figure 11.6. Evolution of the spectral energy distribution (SED) of a stellar population modelled as a star formation burst of 3 Gyr, over the lifetime of the universe. From top to bottom, the SEDs are shown at ages: 0.2, 3.2, 3.4, 4, 5, 10, 18 Gyr. The latest Bruzual and Charlot spectral synthesis models have been used.

of neutral hydrogen clouds along the sightline (Lyα forest) produces a further depression blueward of the Lyα, which becomes stronger at higher redshifts. As a result, a star-forming galaxy at $z \simeq 3$ is seen disappearing in the transition from the B to the U band ('U drop-out'). In general, by measuring colours, such as U–B and B–V, one can select a large sample of galaxies around $z \sim 3$, since these sources will stand out in a colour–colour diagram, having very red U–B colours (lyman limit passing through the two filters) and nearly zero B–V colours (flat spectrum). Such a technique was first successfully applied to ground-based imaging data (e.g. Steidel *et al* 1996), which have the advantage of covering much larger solid angles than the HDF, although they cannot match the photometric accuracy of HST, which is critical to measuring colours accurately.
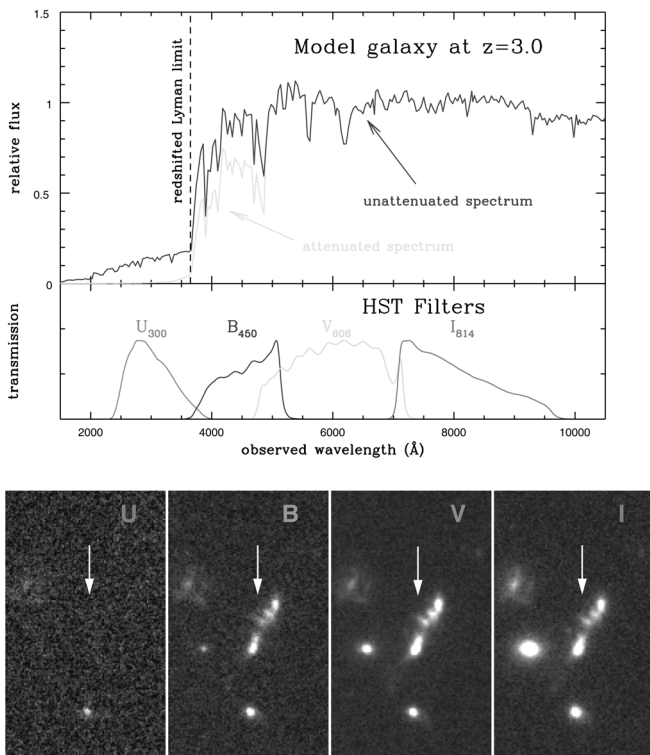
Figure 11.7. Illustration of the Lyman break ('drop-out') technique in the HDF-N from Dickinson (1998). *Top panel*: model spectrum of a star-forming galaxy at $z = 3.0$. Its flat UV continuum (in f_ν units) is truncated by the 912 Å Lyman limit, which is redshifted between the U and B filters of the WFPC2 camera aboard the HST. Intervening neutral hydrogen along the light of sight further suppresses the continuum blueward of Lyα (1216 Å). *Bottom*: HDF-N galaxy, spectroscopically confirmed at $z = 2.8$, as observed in the four WFPC2 bandpasses. Its flux is constant in V and I, it dims in B and completely vanishes in the U-band image.

Follow-up spectroscopy with the Keck telescope has confirmed that objects selected in this fashion were indeed star-forming galaxies at $2 \lesssim z \lesssim 3.5$ (Steidel *et al* 1996). The same technique can be applied to search for higher redshifts galaxies/AGN, for example, objects at $z \gtrsim 4$, the so-called 'B drop-outs' (Steidel *et al* 1999), although it becomes much harder as they become fainter ($R > 24$) and more rare. To date, approximately 900 galaxies have measured with a spectroscopic redshift at $z \simeq 3 \pm 0.5$ and approximately 50 at $4 \lesssim z \lesssim 5$. By exploring relatively large volumes at $z \sim 3$, these studies have taught us much about the star formation density (see section 11.3.5) and large-scale structure (e.g.

Giavalisco *et al* 1998) in the universe back to epochs which represent only 20% of the cosmic time (e.g. Steidel *et al* 1998, 1999).

The Lyman-break technique is just a particular case of a more general method known as *photometric redshifts*. Photometric information from a multi-colour survey can be used as a very low resolution spectrograph to constrain the galaxy SED and thus to estimate the redshift. A good example is shown in figure 11.8 (Giallongo *et al* 1998). A set of SED templates, generally generated with spectral synthesis models (i.e. Bruzual and Charlot models, including UV absorption by the intergalactic medium and dust reddening), is compared with broad photometry data. The best-fit template yields the redshift and the nature of the galaxy.

The photometric redshift technique has been extensively tested in the HDF-N data, since approximately 150 spectroscopic redshifts are available in this field out to $z \simeq 4.5$ and high photometric accuracy can be achieved with the angular resolution and depth of HST images. For example, Benitez (2000) has shown that an accuracy of $\Delta z \leq 0.08(1 + z_{\text{spec}})$ can be reached using a Bayesian estimation method (see figure 11.9). With such an accuracy, one can use photometric redshifts to study the evolution of global statistical properties of galaxy populations, such as clustering at $z \lesssim 1$ and the star formation history out to $z \simeq 4$ (see later).

11.3.5 Star formation history in the universe

The UV continuum of a star-forming galaxy probes the emission from young stars and therefore it directly reflects the ongoing star formation rate (SFR). The optimal wavelength range is ∼1250–2500 Å, longward of the Lyα forest but at wavelengths short enough that the contribution from older stellar populations can be neglected. In order to establish the relationship between SFR and UV luminosity, evolutionary synthesis models are used. This is a multiparameter exercise though. Basic ingredients include: the metallicity of the stars, the star formation history, the IMF, as well as stellar tracks and atmospheres. A series of these constant SF models, with a range input parameters, is shown in figure 11.10 (lower curves). After ∼1 Gyr, the UV luminosity settles around a well defined value which can be used to convert UV luminosities into SFRs. Madau *et al* (1998) used the following relation:

$$\text{SFR}(M_\odot \text{ yr}^{-1}) = 1.4 \times 10^{-28} L_{\text{UV}}(\text{erg s}^{-1} \text{ Hz}^{-1}). \qquad (11.26)$$

For models with a short burst of star formation (upper curves) such a simple relation does not exist, although, statistically speaking, (11.26) is still a reasonable approximation, if a sample of galaxies is caught during their first Gyr of life.

Equation (11.26) applies in the wavelength range 1500–2800 Å since the spectrum f_ν of a star-forming galaxy is nearly flat in that region. At $z \gtrsim 1$ optical observations probe this UV rest frame portion of spectrum, therefore the observed luminosity function, or luminosity density, can be directly converted to
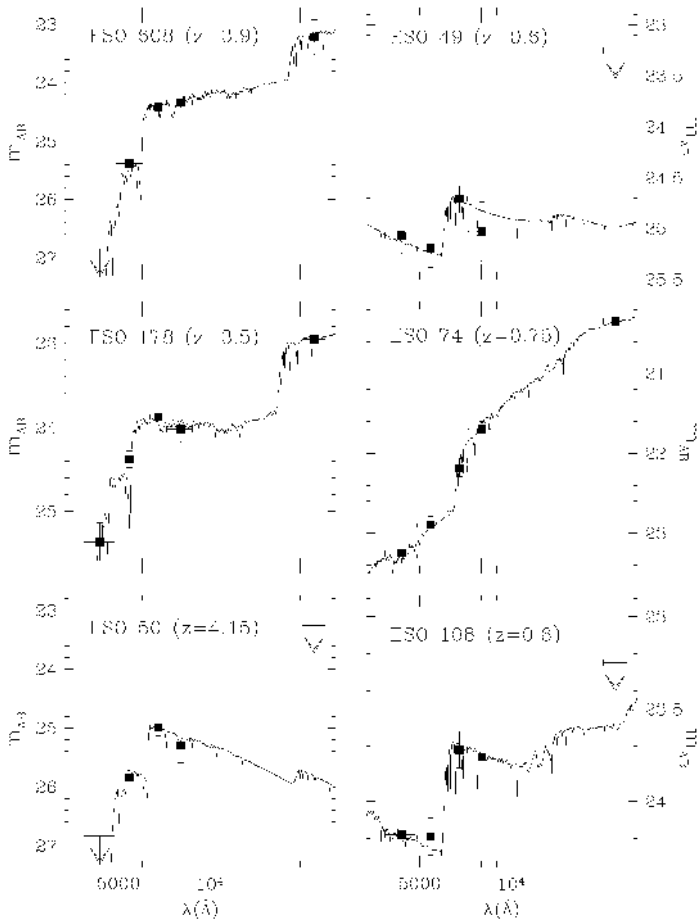
Figure 11.8. Illustration of the photometric redshift technique on a variety of intermediate and high redshift galaxies (Giallongo *et al* 1998). The data points are broad-band photometric meaurements in BVRIK filters used to constrain the spectral energy distribution of galaxies, thus estimating their redshift.

SFR density. By using photometric redshifts (possibly supported by a subset of spectroscopic measurements), one can thus trace the *star formation history* in the distant universe. Madau *et al* (1998) exploited this method to measure the global SFR at $0.5 \lesssim z \lesssim 4$ using HDF and ground-based surveys. This measurement has been repeated by many others in recent years (e.g. Steidel *et al* 1999), and most of the debate has focused on the critical role of *dust* which is surely present in high-*z* galaxies and is very effective in absorbing UV radiation. To some extent all UV-based SFR measurements are biased low due to dust extinction (e.g. Steidel
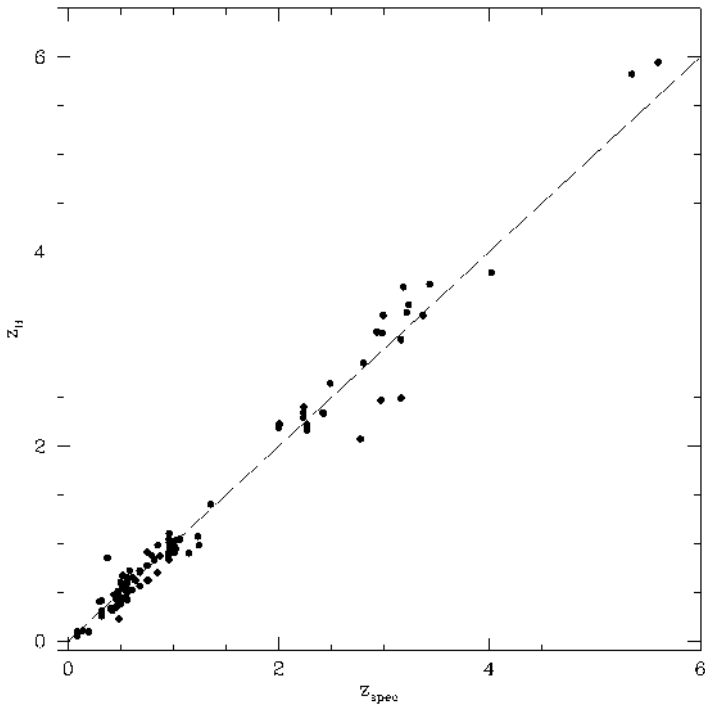
Figure 11.9. Comparison between the spectroscopic redshift (z_{spec}) and the photometric redshift (z_B) in the HDF-N (Benitez 2000).

et al 1999). The standard procedure is to apply statistical corrections, which use empirical correlations of the UV slope β with the extinction derived from the Balmer decrement in nearby starburst galaxies (Calzetti *et al* 1994).

A collection of (mostly dust corrected) estimates of the SFR density over a broad range of redshifts is shown in figure 11.11, which illustrates the great progress made in recent years. This picture seems to suggest that a large fraction of the stars had already been formed by $z \sim 3$. However, global average SFR densities over large cosmic volumes, even in the hypothesis that we can correct for dust extinction, tell us very little about the processes which modulate the star formation (e.g. merging events) and lead to build galaxy masses over time. Future space-based far-infrared (5–30 μm) observations, by providing rest-frame near-IR radiation (which is well correlated with the stellar and dynamical mass) and by measuring the thermally reradiated dust emission in distant galaxy, hold the best promise to shed new light on these issues.
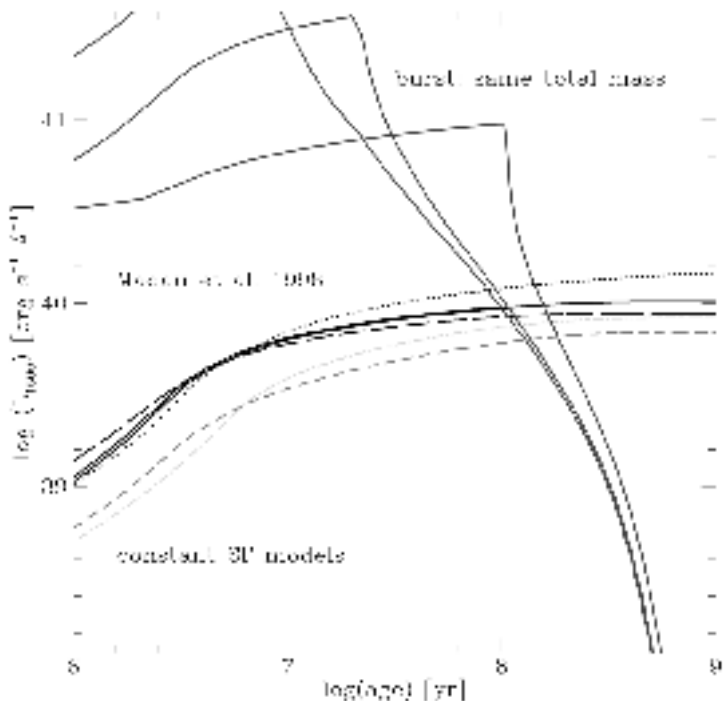
Figure 11.10. Linking the star formation rate (SFR) to the UV luminosity (L_{1500}) using population synthesis models (from Schaerer 1999). Lower curves give the temporal evolution of L_{1500} for models with a constant SFR of $1 M_\odot$ yr^{-1}. Upper curves are models with a burst of SF with duration 5, 20, 100 Myr, forming the same total mass ($10^9 M_\odot$).

11.4 Cluster surveys

11.4.1 Clusters as cosmological probes

The distribution and masses of galaxy clusters are important testing tools for models describing the formation and evolution of cosmic structures. In standard scenarios, clusters form in correspondence with the high peaks (i.e. rare fluctuations) of the primordial density field (e.g. Kaiser 1984). Therefore, both the statistics of their large-scale distribution and their abundance are highly sensitive to the nature of the underlying dark matter density field. Furthermore, their typical scale, $\sim 10 h^{-1}$ Mpc relates to fluctuation modes which are just approaching the nonlinear stage of gravitational evolution. Thus, although their internal gravitational and gas dynamics are rather complex, a statistical description of global cluster properties can be obtained by resorting to linear theory or perturbative approaches. By following the redshift evolution of clusters, we have a valuable method to trace the global dynamics of the universe and, therefore, to determine its geometry.
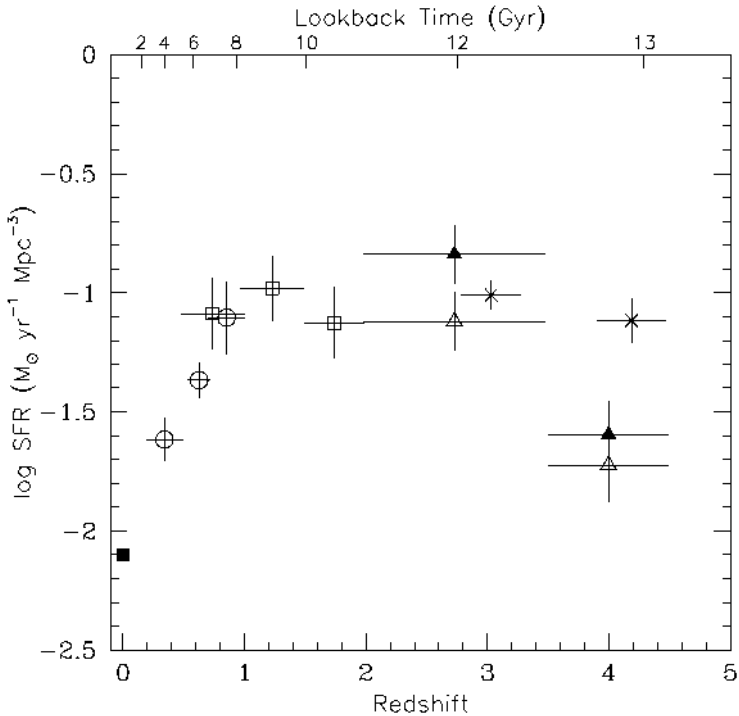
Figure 11.11. History of the star formation rate (SFR) in the universe (∼80% of the cosmic time): SFR density versuss. redshift as derived by the UV luminosity density of different distant galaxy samples (see Ferguson *et al* (2000) for a review). Loopback time and distances are computed using $\Omega_m, \Omega_\Lambda, h = 0.3, 0.7, 0.65$.

In this context, the cluster abundance at a given mass has long been recognized as a stringent test for cosmological models. Typical rich clusters have masses of about $5 \times 10^{14} h^{-1} M_\odot$, i.e. similar to the average mass within a sphere of $\sim 8 h^{-1}$ Mpc radius in the unperturbed universe. Therefore, the local abundance of clusters is expected to place a constraint on σ_8, the rms mass fluctuation on the $8 h^{-1}$ Mpc scale. Analytical arguments based on the approach devised by Press and Schechter (1974) show that the cluster abundance is highly sensitive to σ_8 for a given value of the density parameter Ω_m. Once a model is tuned so as to predict the correct abundance of local ($z \lesssim 0.1$) clusters, its evolution will mainly depend on Ω_m (e.g. Eke *et al* 1996). Therefore, by following the evolution of the cluster abundance with redshift one can constrain the value of the matter density parameter and the fluctuation amplitude level at the cluster scale.

The evolution of cosmic structures, building up in a process of hierarchical clustering, is well illustrated in the VIRGO simulations (Jenkins *et al* 1998) of figure 11.12 (see also the chapter by Anatoly Klypin in this volume). The
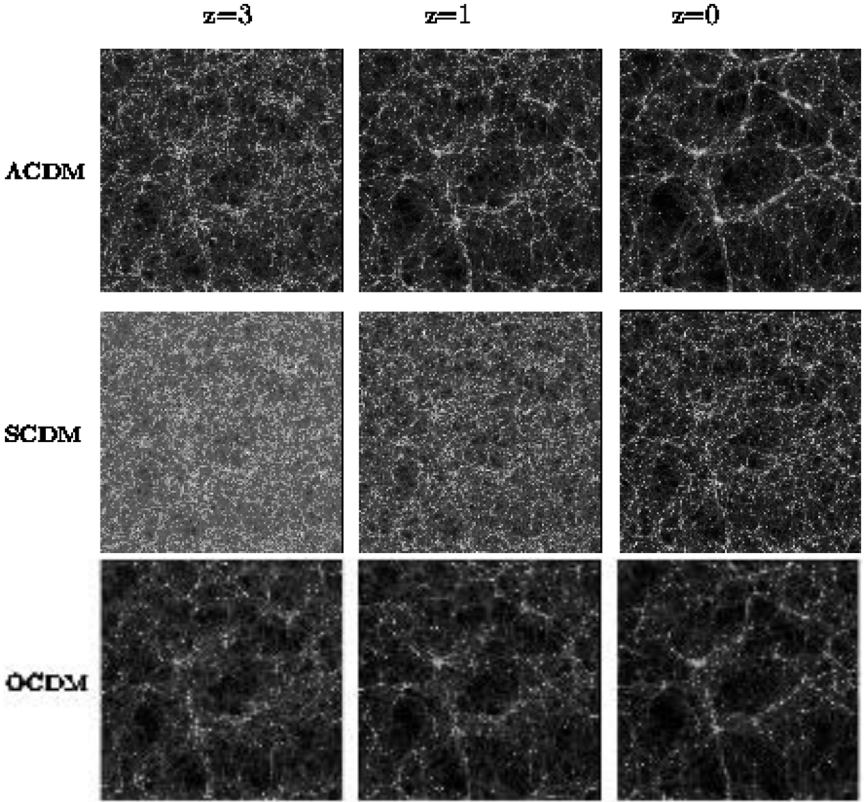
Figure 11.12. Evolution of the cosmic structure (projected mass distribution) from $z = 3$ to the present, as obtained with large N-body simulations by the VIRGO Colloboration (Jenkins *et al* 1998). The three models are Λ-CDM, S(tandard)-CDM and O(pen)-CDM with, respectively, the following parameters $(\Omega_m, \Omega_\Lambda, \Gamma, h) = (0.3, 0.7, 0.21, 0.7), (1, 0, 0.5, 0.5), (0.3, 0, 0.21, 0.7)$. Γ is the shape parameter of the power spectrum. Each box is $240h^{-1}$ Mpc across.

projected mass distribution is shown in three snapshots ($z = 3, 1, 0$), for three different cold dark matter (CDM) models. Model parameters have been chosen to reproduce approximately the same abundance of clusters at $z = 0$ (using a different normalization σ_8). These simulations clearly show that the growth rate of perturbations depends mainly on Ω_m and, to a lesser extent, on Ω_Λ. In low density models, fluctuations start growing in the early universe and stop growing at $1 + z \sim \Omega_m^{-1}$. In SCDM ($\Omega_m = 1$) large structure form much later, and end up evolving rapidly at $z < 1$. The effect of the cosmological constant is to lengthen cosmic time (figure 11.1) and to 'counteract' the effect of gravity, so that perturbations cease to grow at slighly later epochs (a close inspection of

figure 11.12 shows indeed less structure at $z = 3$ in the ΛCDM model when compared with OCDM).

One of the fundamental quantities that a CDM model predicts is the *cluster mass function*, $N(M, z)$, i.e. the number of virialized clusters per unit volume and mass, at different epochs. This can be derived by applying cluster-finding algorithms directly on simulations, as in figure 11.12. A very simple and powerful method proposed by Press and Schechter (1974) is, however, often used to compute $N(M, z)$. This analytical approach is found to be in remarkable agreement with *N*-body simulations, although slight refinements have recently been proposed (Sheth and Tormen 1999). We refer the reader to the original papers or the aforementioned textbooks for a derivation of the Press–Schechter method.

11.4.2   Cluster search methods

The cluster mass is not a direct observable, although several methods exist to estimate the total gravitational mass of clusters. In order to derive the cluster mass function at varying redshifts, one needs three essential tools:

(1) an efficient method to find clusters at least out to $z \simeq 1$;
(2) an estimator (observable), $\hat{M}$, of the cluster mass; and
(3) a simple method to compute the selection function, i.e. the comoving volume within which clusters are found.

We can summarize the methods of finding distant clusters as follows:

- *Galaxy overdensities in optical/IR images*: this is the traditional way which was successfully used by Abell to compile his milestone cluster catalogue. At high redshifts, chance superpositions of unvirialized systems and strong *K*-corrections for cluster galaxies make optical searches very inefficient. Near-IR searches, supported by some colour information, improve substantially the effectivness of this method. In general, however, the estimate of the survey volume is ill defined and model dependent. In addition, the optical luminosity is poorly correlated with the cluster mass.
- *X-ray selected searches*: arguably, the most efficient method used so far to construct distant cluster samples and to estimate the mass function. The x-ray luminosty is well correlated with the mass and the selection function is straightforward, since it is the one of a (x-ray) flux-limited sample. Possible biases, similar to galaxy searches, are connected to possible surface brightness limits.
- *Search for galaxy overdensities around high-z radio galaxies or AGN*: searches are conducted in near-IR or narrow-band filters. This method has provided so far the only examples of possibly virialized systems at $z > 1.5$ (e.g. Pentericci *et al* 2000).
- *Sunyaev–Zeldovich (SZ) effect*: distortion of the CMB spectrum due to the cluster hot intra-cluster medium. Being a detection in absorption,

sensitivity does not depend on redshift. This will possibly be one of the most powerful methods to find distant clusters in the years to come. At present, serendipitous surveys with interferometric techniques (e.g. Carlstrom 1999) cannot cover large areas (i.e. more than ~ 1 deg^2) and their sensitivity is limited to the most x-ray luminous clusters.

- *Clustering of absorption line systems*: this method has lead to a few detections of 'proto-clusters' at $z \gtrsim 2$ (e.g. Francis *et al* 1996). The most serious limitation of this technique is that it is limited to explore small volumes.

To date, the most common procedure used to estimate the cluster mass function has been to exploit x-ray selected samples, for which the survey volume can be computed. Follow-up observations are then used to estimate the cluster mass of a statistical subsample. Most common mass estimators are the temperature of the x-ray emitting gas (directly measured with x-ray spectroscopy), and the galaxy velocity dispersion (virial analysis of galaxy dynamics). We will see later that the x-ray luminosity is also a valid estimator. Gravitational lensing (either in the strong or weak regime) is also a powerful tool to estimate the cluster mass; however, this method is difficult to apply to distant clusters and has some inherent limitations (e.g. mass-sheet degeneracy). For a review of gravitational lensing methods of mass reconstruction, the reader is referred to the chapter by Philippe Jetzer in this volume.

A robust method to quantify the volume density of clusters at different redshifts is to use the x-ray luminosity function (XLF), i.e. the number of clusters per unit volume and per unit x-ray luminosity. By comparing the XLF of an x-ray flux-limited samples of clusters at different redshifts, one can characterize the evolution in luminosity and/or number density. This tool is the exact counterpart of the optical LF used in galaxy surveys (section 11.3.3). Perhaps surprisingly, this standard method applied to cluster surveys has several advantages over galaxy surveys. First, the local XLF is very well determined and no ambiguity exists as from different 'types'. Clusters are basically a single parameter family, the gas temperature, which is also well correlated with the x-ray luminosity. For this reason, K-corrections are also easy to handle as opposed to galaxies in the optical–near-IR. The only point of major concern, as previously discussed, has to do with biases due to surface brightness limits.

In figure 11.13 we show the best determination to date of the XLF from $z \simeq 0$ out to $z \simeq 1.2$, coming from different surveys (Rosati *et al* 1999 and references therein). The most striking result is perhaps the lack of any significant evolution out to $z \simeq 1$, for $L_X \lesssim L_X^* \simeq 5 \times 10^{44}$ erg s^{-1} (i.e. approximately the Coma cluster). This range of luminosities includes the bulk of the cluster population in the universe. However, there is evidence of evolution of the space density of the most luminous, presumably most massive clusters. Using the observed $L_X - T$ relation for clusters and the virial theorem, which links the temperature to the mass, one can show that the XLF can be used as a robust estimator of the cluster
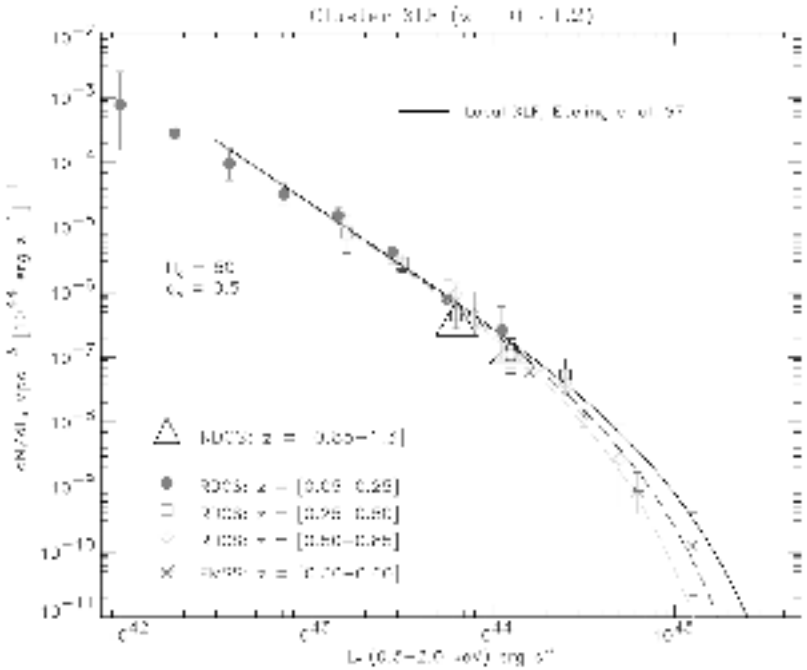
Figure 11.13. The best determination to date of the cluster x-ray luminosity function (i.e. the cluster space density) out to $z \simeq 1.2$. Data points at $z < 0.85$ are derived from a complete RDCS sample of 103 clusters over 47 deg^2, with $F_{X_{lim}} = 3 \times 10^{-14}$ erg s^{-1} cm^{-2} (Rosati *et al* 1999). The triangles represent *a lower limit* (due to incomplete optical identification). to the cluster space density obtained from a fainter and more distant subsample. Long dash curves are Schechter best fits to the XLF $\phi(L_X, z)$, plotted at $z = 0.4$ and $z = 0.6$.

mass function, i.e. $N(L_X, z) \rightarrow N(T, z) \rightarrow N(M, z)$ (e.g. Borgani *et al* 1999). Such a method can be used to set significant constraints on Ω_m (figure 11.14). The fact that a large fraction of relatively massive clusters is already in place at $z \simeq 1$, indicates that the dynamical evolution of structure has proceeded at a relatively slow pace since $z \simeq 1$, a scenario which fits naturally in a low density universe (figure 11.14, see Borgani *et al* 2001, Eke *et al* 1996).

11.4.3 Determining Ω_m and Ω_Λ

Besides the method of the evolution of cluster abundance (which we can call 'universal dynamics'), galaxy clusters, as the largest collapsed objects in the universe, also offer two other independent means to estimate the mean density of matter that participates to gravitational clustering (i.e. Ω_m):
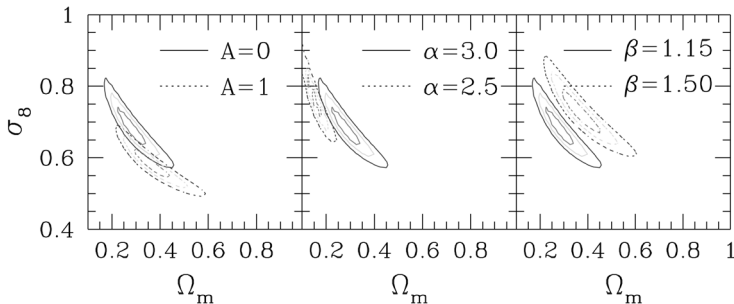
Figure 11.14. Constraints in the plane of the cosmological parameters $\Omega_m - \sigma_8$ derived from the observed evolution of the cluster abundance in the RDCS sample (Borgani *et al* 2001). Contours are 1σ, 2σ and 3σ C.L. The three parameters (A, α, β) describe the uncertainties in converting cluster masses into temperatures ($T \sim M^{2/3}/\beta$), and temperatures into x-ray luminosities ($L_X \sim T^\alpha (1 + z)^A$). The two values for each parameter bracket the range which is allowed from current x-ray observations of distant clusters.

(1) $\Omega_b - f_{gas}$ method,
(2) Oort method (M/L) and
(3) universal dynamics.

11.4.3.1 $\Omega_b - f_{gas}$ method (White et al 1993)

A reasonable assumption is that clusters are large enough that they should host a 'fair sample' of the matter in the universe (e.g. there is no special segregation of baryons over the dark matter). In addition, x-ray observations clearly show that most of the baryons in clusters reside in the hot intracluster gas. The gas-to-total-mass ratio, f_{gas}, can be measured using x-ray or SZ observations. The fraction of baryons, $\Omega_b = \rho_B/\rho_{cr}$, is well constrained by the primordial nucleosynthesis theory and the measurement of deuterium abundance from high-z absorption systems. If we know f_{gas} and Ω_b, then we simply have: $\Omega_m = \Omega_b/f_{gas}$.

Deuterium measurements in recent years have settled on the value (Burles and Tytler 1998) $\Omega_b h^2 = 0.02 \pm 0.002$. Ettori and Fabian (1999) have used 36 x-ray clusters to estimate a mean value $\langle f_{gas} \rangle = 0.059 h^{-3/2}$ with a 90% range of $f_{gas} = (0.036–0.087) h^{-3/2}$. Hence,

$$\Omega_m = \Omega_B/f_{gas} \simeq 0.34 h^{-1/2} \simeq 0.4 \pm 0.2 \qquad \text{(for } H_0 = 65), \qquad (11.27)$$

where the error represents an approximate range reflecting the scatter in f_{gas}.

11.4.3.2 Oort method (M/L)

The mean density of the universe is equal to the mass of a large galaxy cluster divided by the equivalent comoving volume in the field from which that mass
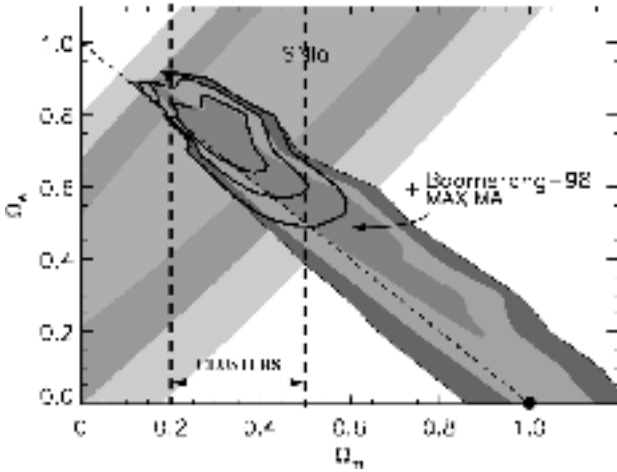
Figure 11.15. Constraints to Ω_m and Ω_Λ from CMB anisotropies (Boomerang: De Bernardis *et al* 2000; Maxima: Hanany *et al* 2000), distant Type Ia supernovae (Perlmutter *et al* 1999; Schmidt *et al* 1998) and several methods based on galaxy clusters.

originated. Such a volume can be evaluated from the ratio of the luminosity of the cluster galaxies, L, with the *field luminosity density*, j_f. Thus,

$$\rho_0 = M_{cl}/V_{cl} = (M/L)_{cl} \times j_f, \qquad \text{and} \qquad \Omega_m = (M/L)_{cl}/(M/L)_{cr} \quad (11.28)$$

where $(M/L)_{cr} = \rho_{cr}/j_f$.

Important effects which could bias this measurement are luminosity segregation of the cluster versus the field, and differential evolution of the cluster galaxies compared to the field. With enough spectrophotometric data, one can reasonably control these issues. The CNOC survey (e.g. Carlberg *et al* 1996) is the best study to date of cluster dynamics of an x-ray selected sample of 16 clusters *at $z \lesssim 0.5$*. This study lead to a measurement of average mass-to-light ratio $(M/L) = 295 \pm 54 \, h \, M_\odot L_\odot^{-1}$, as well as of the luminosity density j_f in the field. Thus, Carlberg *et al* obtain: $\Omega_m = 0.24 \pm 0.05 \pm 0.09$ (the second error is the sytematic one).

Using the constraint on Ω_m derived in the previous section from the application of the third method (universal dynamics), we note a remarkable agreement from *completeley independent techniques* based on galaxy clusters, i.e. $\Omega_m \simeq 0.2$–0.5.

These bounds on the matter density parameter are shown in figure 11.15 together with measurements of $(\Omega_m, \Omega_\Lambda)$ from high redshift supernovae used as standard candles (Perlmutter *et al* 1999, Schmidt *et al* 1998), and from the recent landmark experiments—Boomerang (De Bernardis *et al* 2000) and Maxima (Hanany *et al* 2000) which have measured CMB anisotropies on small

scales (see the chapter by Arthur Kosowsky in this volume). The power of these three independent means of measuring $(\Omega_m, \Omega_\Lambda)$ is that they have degeneracies which lie almost orthogonally to each other. The directions of degeneracy in the $(\Omega_m, \Omega_\Lambda)$ plane can be written as

$$\text{SN: } \tfrac{4}{3}\Omega_m - \Omega_\Lambda \simeq \text{constant} \qquad \text{CMB: } \Omega_m + \Omega_\Lambda \simeq \text{constant}$$
$$\text{clusters: } \Omega_m \simeq \text{constant.}$$

These three measurements of the cosmological parameters are well in agreement with each other and define a relatively small allowed region, a circumstance which is sometimes referred to as 'cosmic concordance' (Bahcall *et al* 1999). This explains why by 'standard cosmology' these days one adopts the values $(\Omega_m, \Omega_\Lambda) = (0.3, 0.7)$. Interestingly, the age of the universe for this model is $T_U = 0.965 H_0^{-1}$.

References

Bahcall N, Ostriker J P, Perlmutter S and Steinhardt P J 1999 *Science* **284** 1481

Benitez M 2000 *Astrophys. J.* **536** 571

Borgani S, Rosati P, Tozzi P and Norman C 1999 *Astrophys. J.* **517** 40

Borgani S *et al* 2001 *Astrophys. J.* **559** L71

Bruzual A G and Charlot S 1993 *Astrophys. J.* **405** 538

Burles S and Tytler D 1998 *Astrophys. J.* **507** 732

Calzetti D, Kinney A L and Storchi-Bregmann T 1994 *Astrophys. J.* **429** 582

Carlberg *et al* 1996 *Astrophys. J.* **462** 32

Carlstrom J S 1999 *Phys. Scr.* ed L Bergstrom, P Carlson and C Fransson

Colless M M 1999 *Proc. 'Looking Deep in the Southern Sky' (ESO Astrophysics Symposia)* ed R Morganti and W J Couch (Berlin: Springer) p 9

Cowie L L, Sonfalia A, Hu E M and Cohen J D 1996 *Astron. J.* **112** 839

Dickinson M 1998 *Proc. STScI May 1997 Symposium 'The Hubble Deep Field'* ed M Livio, S M Fall and P Madau *Preprint* astro-ph/9802064

de Bernardis P *et al* 2000 *Nature* **404** 955

Driver S P, Fernandez-Soto A, Couch W J, Odewahn S C, Windhorst R A, Phillipps S, Lanzetta K and Yahil A 1998 *Astrophys. J.* **496** L93

Eke R *et al* 1996 *Mon. Not. R. Astron. Soc.* **282** 263

Ellis R G, Colless M, Broadhurst T J, Heyl J S and Glazebrook K 1996 *Mon. Not. R. Astron. Soc.* **280** 235

Ellis R G 1997 *Annu. Rev. Astron. Astrophys.* **35** 389

Ettori S and Fabian A C 1999 *Mon. Not. R. Astron. Soc.* **305** 834

Ferguson H C, Dickinson M and Williams R 2000 *Annu. Rev. Astron. Astrophys.* **38** 667

Giallongo E, D'Odorico S, Fontana A, Cristiani S, Egami E, Hu E and McMahon R G 1998 *Astron. J.* **115** 2169

Giavalisco M, Steidel C C, Adelberger K L, Dickinson M, Pettini M and Kellogg M 1998 *Astrophys. J.* **503** 543

Hanany S *et al* 2000 *Astrophys. J.* **545** L5

Hu E M, McMahon R G and Cowie L L 1999 *Astrophys. J.* **522** L9

Hubble E 1926 *Astrophys. J.* **64** 321

Huchra J P, Geller M J, de Lapparant V and Corwin H G 1990 *Astrophys. J. Suppl.* **42** 433

Jenkins *et al* 1998 *Astrophys. J.* **499** 20

Kaiser N 1994 *Astrophys. J.* **284** L9

Kellermann K I 1993 *Nature* **361** 134

Landau L D and Lifshitz E M 1971 *The Classical Theory of Fields* (Oxford: Pergamon)

Longair M S 1998 *Galaxy Formation* (Berlin: Springer)

Lilly S J, Tresse L, Hammer F, Crampton D and LeFevre O 1995 *Astrophys. J.* **455** 108

Loveday J, Peterson B A, Efstathiou G and Maddox S J 1992 *Astrophys. J.* **390** 338

Madau P, Pozzetti L and Dickinson M 1998 *Astrophys. J.* **498** 106

Maddox S J, Efstathiou G, Sutherland W J and Loveday J 1990 *Mon. Not. R. Astron. Soc.* **247** 1

Pentericci L *et al* 2000 *Astron. Astrophys.* **361** L25

Peacock J A 1999 *Cosmological Physics* (Cambridge: Cambridge University Press)

Peebles P J E *Principles of Physical Cosmology* (Princeton, NJ: Princeton University Press)

Perlmutter S *et al* 1999 *Astrophys. J.* **517** 565

Press W H and Schechter P 1974 *Astrophys. J.* **187** 425

Rosati P, Della Ceca R, Burg R, Norman C and Giacconi R 1998 *Astrophys. J.* **492** L21

Rosati *et al* 1999 *Proc. 'Large Scale Structure in the X-ray Universe'* ed M Plioniz and I Georgantopoulos (Greece: Santorini) (astro-ph/0001119)

Sandage A 1995 *The Deep Universe (Saas-Fee Advanced Course 23)* (Berlin: Springer)

Schaerer D 1999 *Proc. XIXth Moriond Astrophysics Meeting 'Building the Galaxies: from the Primordial Universe to the Present'* ed Hammer *et al* (Paris: Editions Frontières) (astro-ph/9906014)

Schechter P 1976 *Astrophys. J.* **203** 297

Shectman S A *et al* 1996 *Astrophys. J.* **470** 172

Sheth R K and Tormen G 1999 *Mon. Not. R. Astron. Soc.* **308** 119

Schmidt B P *et al* 1998 *Astrophys. J.* **507** 46

Steidel C C, Giavalisco M, Dickinson M and Adelberger K L 1996 *Astrophys. J.* **462** L17

Steidel C C, Adelberger K L, Dickinson M, Giavalisco M, Pettini M and Kellogg M 1998 *Astrophys. J.* **492** 428

Steidel C C, Adelberger K L, Giavalisco M, Dickinson M and Pettini M 1999 *Astrophys. J.* **519** 1

Tyson J A 1988 *Astron. J.* **96** 1

White S D M, Navarro J F, Evrard A E and Frenk C S 1993 *Nature* **366** 429

Yee H K C *et al* 2000 *Astrophys. J. Suppl.* **129** 475 (astro-ph/0004026)